

Check for updates

Macro-Superlubricity Induced by Tribocatalysis of High-Entropy Ceramics

Changhe Du, Tongtong Yu, Xudong Sui, Zhengfeng Zhang, Rongsheng Cai, Liqiang Zhang, Yange Feng, Min Feng, Feng Zhou, and Daoai Wang*

Macroscale superlubricity has attracted considerable attention as a promising strategy to minimize frictional energy dissipation and achieve near-zero wear. However, realizing macroscale superlubricity with prolonged durability remains an immense challenge, particularly on engineering steels. Current superlubricants render steel surfaces susceptible to corrosion, causing severe wear and superlubrication failure. Herein, high-entropy ceramics (HEC) with catalytic properties are innovatively introduced to prevent corrosion of engineering steels and achieve macro-superlubricity through tribo-catalytic effect. Furthermore, this catalytically induced superlubricity system exhibits an ultra-low friction coefficient of 0.0037 under contact pressure up to 1.47 GPa, an ultra-long cycle lifetime of 1.25×10^6 cycles (corresponding sliding distance up to 5 km), and an extremely low wear rate of 3.032×10^{-10} mm³·N⁻¹·m⁻¹ on the HEC surface. Based on the experimental analysis and theoretical simulation, the in situ formed HEC nanocrystals reduce the Gibbs free energy of hydrolysis of PA molecules into inositol and phosphoric acid molecules in the lubricant. Notably, the hydrolysis products favorably contributed to the reduction of shear force in the lubrication system, which is essential for achieving macroscale superlubricity over a long time. This study provides a new perspective for designing robust superlubricity systems by harnessing the tribocatalytic effect of high-entropy materials.

C. Du, T. Yu, X. Sui, Z. Zhang, R. Cai, L. Zhang, Y. Feng, M. Feng, F. Zhou, D. Wang

State Key Laboratory of Solid Lubrication
Lanzhou Institute of Chemical Physics

Chinese Academy of Sciences Lanzhou 730000, China

E-mail: wangda@licp.cas.cn

C. Du, T. Yu, Z. Zhang, R. Cai, Y. Feng, F. Zhou, D. Wang Center of Materials Science and Optoelectronics Engineering University of Chinese Academy of Sciences

Beijing 100049, China

C. Du, Y. Feng, M. Feng, D. Wang

Shandong Laboratory of Yantai Advanced Materials and Green Manufacturing

Yantai 265503, China

1aiitai 205505, Ciii

X. Su

Institute for Engineering Design and Product Development Tribology Research Division

TU Wien

Vienna 1060, Austria



DOI: 10.1002/adma.202413781

1. Introduction

Friction and wear in mechanical motion systems lead to substantial energy consumption, shorten the service life of industrial components, and cause severe material and economic losses.[1] Superlubricity (friction coefficient less than 0.01) has garnered significant research interest in recent years and offers a viable solution for substantially reducing fuel consumption and carbon dioxide emissions.[2] Through the concerted efforts of researchers, the realization of superlubricity has transitioned from theoretical studies at the microscopic scale to practical applications at the macroscopic level.[3] Solid lubricating films, based on incommensurate contact interfaces and weak interlayer interactions, have exhibited exceptional superlubricity performance.[4] However, limited by the severe applied conditions and susceptible to wear, solid superlubricity films were difficult to apply in practical engineering conditions under an atmospheric environment.[5]

In contrast to solid superlubricity, liquid lubricants are more amenable to

achieving macroscopic superlubricity under atmospheric conditions, rendering them promising candidates for the engineering applications of superlubricity technology.^[6] Among them, waterbased lubricants, such as acidic solutions or polyol solutions, have demonstrated superlubricating performance due to their weak shear resistance and suitable viscosity indices.[7] Unfortunately, water-based superlubricants usually easy to cause corrosion on the surface of engineering steel and take an extended running-in period.[8] To address the limitations of both solid and liquid superlubricity, strategies that leverage the synergistic effects between solid thin films and liquid lubricants to enhance superlubricity performance have been proposed. [9] For instance, unsaturated fatty acids, exemplified by oleic acid, can decompose on DLC thin films under frictional conditions, forming dense tribofilms and enabling superlubricity.[10] Additionally, glycerol or 3-hydroxypropionic acid can trigger superlubricity on DLC thin films, attributed to the formation of hydroxyl-terminated surfaces or the adsorption of carboxylic acid groups.^[10a,11] Although the development of these solid-liquid composite superlubricating systems is encouraging, the load-carrying capacity of the lubricants and the mechanical properties of the thin films are

1521495.0, Downloaded from https://onlinelibtrary.wiley.com/doi/10.1002/adma.202413781 by Subboleth-memer@advancebelochina.com, Wiley Online Library on [30/11/2024]. See the Terms and Conditions (https://onlinelibtrary.wiley.com/terms-and-conditions) on Wiley Online Library for rules of use; OA articles are governed by the applicable Centwise Commons is a conditions.

relatively low, inevitably leading to wear on the film surfaces and compromising the robustness of superlubricity.

To achieve superlubricity with prolonged durability on engineering steel, on the one hand, it is paramount to design solid thin film materials exhibiting exceptional wear resistance and corrosion resistance, and on the other hand, it is necessary to promote the chemical reaction between the lubricant and the solid film. The mechanically robust thin films can effectively mitigate wear during frictional sliding and withstand indentation or deformation under high contact pressures. When deposited on steel substrates, such protective coatings also effectively prevent corrosion in water-based lubrication environments. [9a,12] Notably, the tribochemical interactions between the lubricant and the solid film play a crucial role in enabling superlubricity. The products of these tribochemical reactions can form boundary-adsorbed films or tribofilms at the contact interfaces, thereby minimizing wear and ensuring the sustainability of the superlubricity system.^[13] Enhancing the chemical reactivity of the sliding interfaces or employing solid films with inherent catalytic properties can significantly accelerate the tribochemical reaction kinetics. [2c,14] Consequently, the design of solid thin films that synergistically combine superior wear resistance and tribocatalytic properties can not only effectively mitigate wear but also promote favorable tribochemical reactions, thereby maximizing the operational lifetime and performance of the superlubricity system. The new high-entropy materials composed of five or more metallic or nonmetallic elements in near-equimolar ratios provide the possibility for this kind of compound lubrication design induced by tribochemical reaction.^[15] Due to the synergistic effects of the highentropy effect, lattice distortion effect, sluggish diffusion effect, and "cocktail" effect, high-entropy materials exhibit exceptional corrosion resistance and mechanical strength.[16] Compared to conventional high-entropy alloys, high-entropy nitride ceramics demonstrate further enhanced wear resistance owing to the solidsolution strengthening effect of the nitrogen element.[17] For instance, Feng et al. found that a (CrTaNbMoV)N thin film with 20% nitrogen content showed the highest hardness (21.6 GPa), and the wear rate of the film decreased by 6 times compared to a CrTaNbMoV metal film.[18] In our previous studies, we also investigated the effects of nitrogen flow rate and substrate bias on the microstructure and mechanical properties of (CrNbTiAlV)N films.[19] We found that nitride films deposited with a nitrogen flow rate of 38 sccm exhibited the best friction-corrosion performance in artificial seawater. [17c] Interestingly, high-entropy ceramic (HEC) nanoparticles have been proven to possess superior chemical catalytic activity, ascribed to their high specific surface area and abundance of catalytically active sites.^[20] Yang et al. prepared HEC nanomaterials using pulsed laser irradiation, and the CoCrFeNiAl HEC electrode demonstrated outstanding activity and stability in the oxygen evolution reaction. [20a] Zhai et al. suggested that compared to single-element catalysts, high-entropy materials offer multi-element active sites, unsaturated coordination, and entropy stabilization, showing promising applications in the field of electrochemical water splitting.^[21] In conclusion, HEC provides an excellent material choice for investigating the realization of robust superlubricity with negligible wear rates through the tribocatalysis effect.

Herein, a new strategy of solid–liquid composite superlubrication in an atmospheric environment was proposed by using the

tribocatalytic effect of natural organic acid phytic acid (PA) and HEC to realize robust superlubrication on the surface of engineering steel. The (CrNbTiAlV)N HEC thin film was designed and deposited on engineering steel substrates via magnetron sputtering with a high hardness of 26.43 GPa and an elastic modulus of 276.46 GPa. The PA was employed as the lubricant and introduced onto the (CrNbTiAlV)N surface to construct a solidliquid composite superlubricity system. Strikingly, this composite lubrication system could sustain a superlubricity state for at least 1.25 million reciprocating friction cycles, maintaining an ultra-low friction coefficient of ≈0.0037 and an exceptionally low wear rate of $3.032 \times 10^{-10} \text{ mm}^3 \cdot \text{N}^{-1} \cdot \text{m}^{-1}$. Post-tribotest characterization revealed the in situ formation of HEC nanocrystals with an average size of \approx 7.3 nm during the frictional process. These nanocrystals facilitated the accelerated hydrolysis of PA molecules into inositol polyphosphate (inositol) and phosphoric acid molecules. Notably, molecular dynamics simulations elucidated that inositol and phosphoric acid further mitigated frictional resistance during sliding, thereby crucially contributing to the macroscopic realization of solid-liquid composite superlubricity. This work demonstrates a viable strategy for achieving robust superlubricity with ultra-low wear rates by harnessing the tribocatalysis effect of HECs.

2. Results and Discussion

2.1. Preparation and Characterization of (CrNbTiAlV)N Film

The (CrNbTiAlV)N thin film was fabricated onto a steel substrate using a magnetron sputtering method, as described in Figure 1a. A splicing target comprising Cr, Nb, Ti, Al, and V was employed as the sputtering source, with nitrogen gas acting as the reactive gas. In addition, the CrNbTiAlV high-entropy alloy film without nitrogen was also prepared for comparison. Notably, a Cr intermediate layer was initially deposited on the substrate surface to bolster the adhesion between the film and the substrate. Detailed fabrication methods and process parameters are provided in the Experimental Section (Figure \$1 and Table \$1, Supporting Information). As shown in Figure 1b, the grazing incidence X-ray diffraction (GIXRD) pattern of the CrNbTiAlV film shows broad diffuse scattering, indicative of its amorphous structure, aside from the diffraction peak of the Cr transition layer at 44.4°. Conversely, the GIXRD pattern of the (CrNbTiAlV)N film reveals four distinct diffraction peaks that are assigned to (111), (200), (220), and (311) planes, suggesting that the prepared (CrNbTiAlV)N film possesses an FCC crystal structure. Five metal elements, Cr. Nb, Ti, Al, and V, randomly occupy the lattice positions and Nitrogen (N) atoms fill the octahedral interstitial sites of the FCC lattice. In other words, the N element exists as an interstitial solute within the solid solution of the highentropy alloy (Figure S2, Supporting Information).[17c,22] To ascertain the thickness, elemental composition, and microstructure of the (CrNbTiAlV)N film, focused ion beam (FIB) milling combined with cross-sectional TEM was used to indicate that the thickness of (CrNbTiAlV)N film is ≈713 nm with a fairly dense structure (Figure 1c). As illustrated in Figure 1d and Figure S3 (Supporting Information), the elemental distribution map shows a uniform dispersion of Cr, Nb, Ti, Al, V, and N elements at the microscopic scale, indicating the formation of a solid solution

15214095, 0, Downloaded from https://onlinelibrary.wiley.com/doi/10.1002/adma.202413781 by

com, Wiley Online Library on [30/11/2024]. See the Terms

onditions) on Wiley Online Library for rules of use; OA articles are governed by the applicable Creative Con

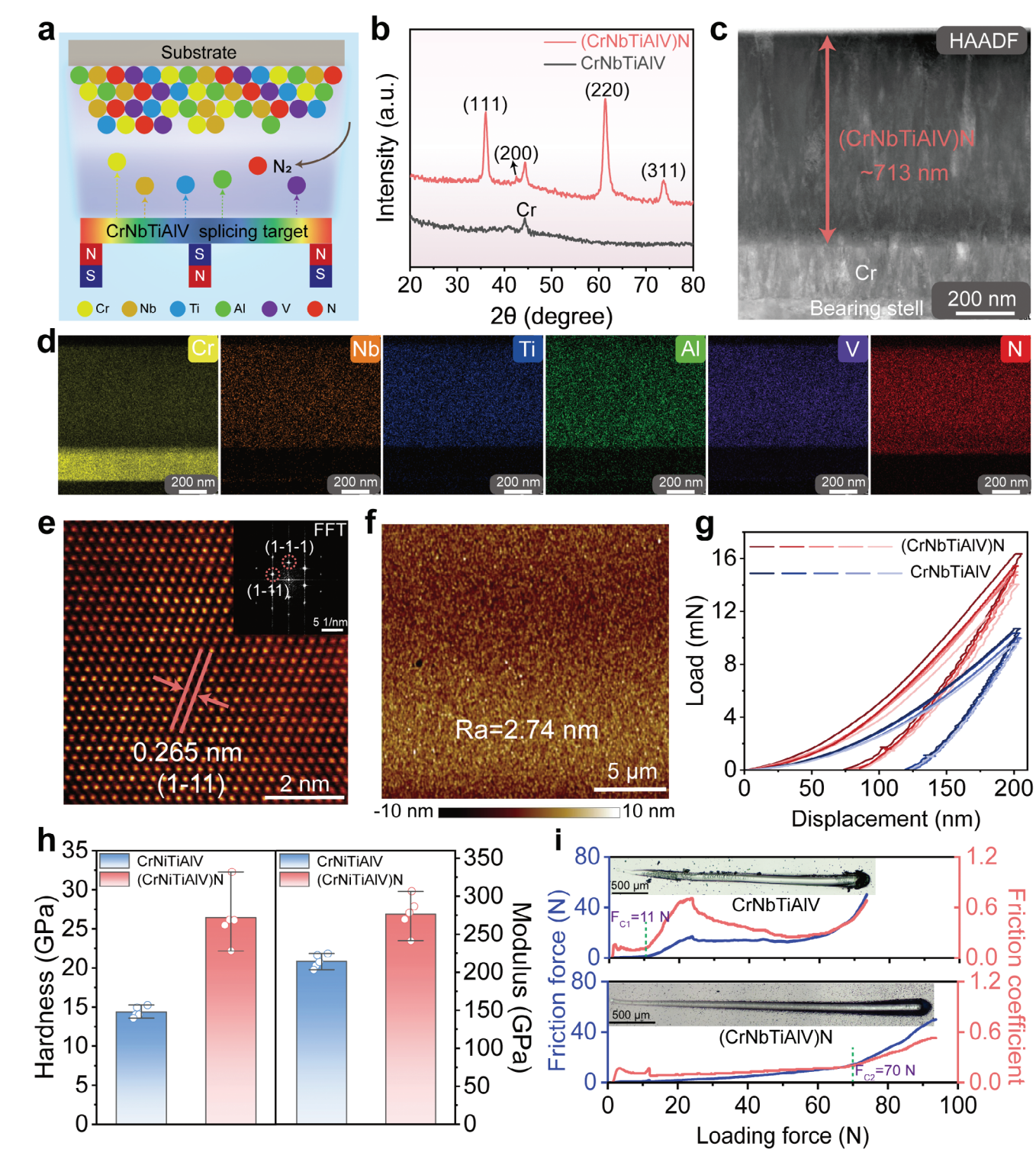


Figure 1. Preparation and characterization of (CrNbTiAlV)N film. a) Schematic diagram of the process of depositing (CrNbTiAlV)N film using the magnetron sputtering method. b) GIXRD patterns of (CrNbTiAlV)N and CrNbTiAlV films (incidence angle is 1°). c) HAADF image and d) EDS elemental mapping results of the cross-section of the (CrNbTiAlV)N film. e) HRTEM image of the cross-section of the (CrNbTiAlV)N film, and the inset in the upper right corner is the corresponding FFT image. f) AFM image showing the surface micromorphology of (CrNbTiAlV)N film. g) Loading–unloading curves of (CrNbTiAlV)N and CrNbTiAlV films measured using a nanoindentation instrument. Five different spot locations were tested for each sample. h) Comparison of hardness and elastic modulus of (CrNbTiAlV)N and CrNbTiAlV films. i) Classic scratch tests were performed on (CrNbTiAlV)N and CrNbTiAlV films to evaluate their adhesion to the substrate. The critical force F_c represents the exposure of the substrate. The inset shows the scratch morphology of the corresponding film.

www.advancedsciencenews.com



www.advmat.de

15214055, O. Downloaded from https://onlinelblaray.wiley.com/doi/10.1002/adma_202413781 by -Shbboletb--member@advancebolchina.com, Wiley Online Library on [301110204]. See the Terms and Conditions (https://onlinelblaray.wiley.com/terms-and-conditions) on Wiley Online Library for rules of use; OA articles are governed by the applicable Centwive Commons in

phase without phase segregation. The EDS and specific elemental contents at the selected area of the (CrNbTiAlV)N film cross-section can be found in Figure S4 (Supporting Information). Furthermore, the periodic crystal structures by high-resolution TEM (HRTEM) and symmetric diffraction spots obtained by using fast Fourier transformation (FFT) demonstrate the face-centered cubic crystal structure of the (CrNbTiAlV)N film, which is consistent with the XRD results (Figure 1e). The lattice fringes spaced at 0.265 nm are attributed to the (1–11) crystal plane. [17a,23] Further confirming the roughness of (CrNbTiAlV)N film was determined to be merely 2.74 nm by using atomic force microscopy (AFM), as shown in Figure 1f.

To accurately evaluate the mechanical properties of the deposited films, load-displacement curves for both CrNbTiAlV and (CrNbTiAlV)N films were obtained using a nanoindentation tester. Figure 1g demonstrates that the (CrNbTiAlV)N film requires a larger external load for the same indentation depth (200 nm) than the CrNbTiAlV film. The plastic deformation region of the (CrNbTiAlV)N film is narrower, indicating that the doping of N elements imparts the nitride film with superior resistance to plastic deformation.^[19] Concurrently, the emergence of a solidsolution phase and the refinement of the grain size endow the (CrNbTiAlV)N film with elevated hardness (26.43 GPa) and elastic modulus (276.46 GPa) (Figure 1h).[24] Combining the AFM and nanoindentation results, it can be inferred that the extremely smooth and hard surface of the (CrNbTiAlV)N film enhances the feasibility of superlubricity, thus contributing to a durable superlubricity condition. In addition, scratch tests were performed on both films to investigate the interfacial bonding strength between the film and the substrate. Throughout the tests, the film initiates delamination from the substrate at the critical load (F_c), accompanied by a substantial shift in the real-time friction coefficient. As shown in Figure 1i, the critical load for the (CrNbTiAlV)N film ($F_{c2} = 70 \text{ N}$) markedly surpasses that of the CrNbTiAlV film $(F_{c1} = 11 \text{ N})$. Within the scratch of the CrNbTiAlV film, there are many transverse cracks and apparent film peeling, whereas the (CrNbTiAlV)N film reveals only minor transverse cracks and no evident brittle flaking. The corresponding enlarged images of the scratch morphology can be found in Figure S5 (Supporting Information). These findings imply a significant enhancement in interfacial adhesion and wear resistance following nitriding.

2.2. Robust Macroscale Superlubricity Behavior of (CrNbTiAlV)N Film and PA Solution

The prepared (CrNbTiAlV)N film exhibits remarkable mechanical properties and possesses a high density of reactive sites on its surface, rendering it a promising candidate for tribochemical reactions and the attainment of macroscopic superlubricity. Subsequently, real-time friction coefficients of the phytic acid (PA) solution were obtained using a ball-on-disk tribometer, as depicted in Figure 2a. The detailed chemical structure of PA is illustrated in Figure S6 (Supporting Information). The upper and lower friction pairs consisted of ceramic or steel balls and bearing steel blocks coated with (CrNbTiAlV)N thin films, respectively. Moreover, to investigate effective lubricating components, friction coefficients were also measured for 51 200 steel and CrNbTiAlV film surfaces lubricated with a PA solution, and

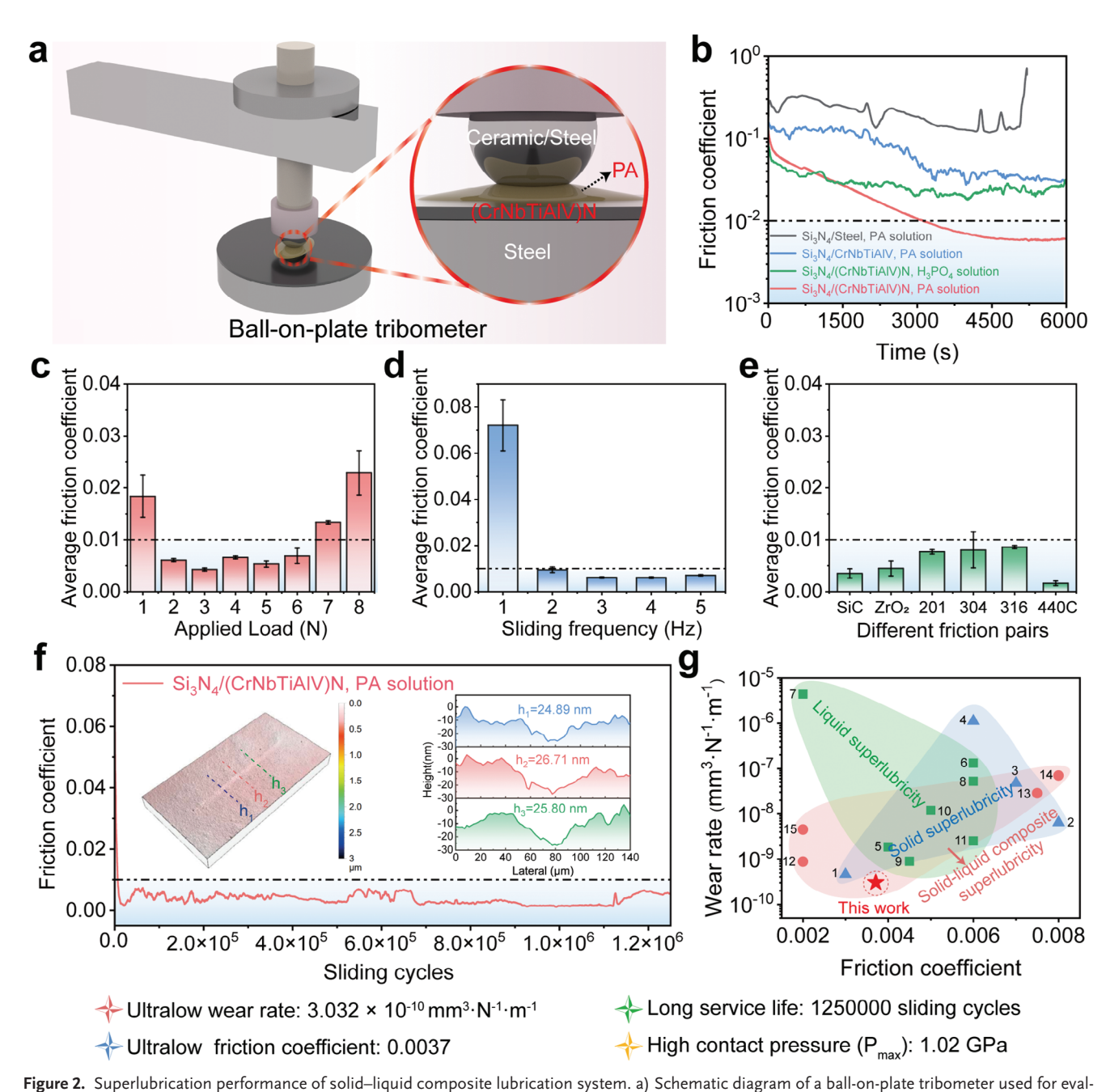
(CrNbTiAlV)N film surfaces lubricated with a phosphoric acid solution. Figure 2b presents the real-time friction coefficient curves for these four distinct composite lubrication systems. On the surface of the bearing steel without the deposited high-entropy alloy coating, the friction coefficient of the PA solution rapidly escalated from 0.138 to 0.708 after \approx 5000 s, reaching the protection threshold set by the tribometer and causing its cessation. This abrupt increase in friction coefficient was attributed to the corrosion of the bearing steel and thus a substantial increase in surface roughness in the acidic PA solution (Figure S7, Supporting Information). After a running-in period of ≈3000 s, the friction coefficients of the CrNbTiAlV thin film lubricated with the PA solution and the (CrNbTiAlV)N thin film lubricated with the phosphoric acid solution stabilized at ≈0.036 and 0.023, respectively. This indicates that neither of these solid-liquid composite lubrication systems achieved macroscopic superlubricity during the 6000 s tribological test.

Intriguingly, the friction coefficient corresponding to the (CrNbTiAlV)N film lubricated with the PA solution (hereafter referred to as PA@(CrNbTiAlV)N) gradually decreased to below 0.01 after a running-in period of \approx 3120 s. As the friction test progressed, the friction coefficient stabilized ≈0.006. This indicates that macroscopic superlubricity can only be achieved through the combined effect of the PA lubricant and the (CrNbTiAlV)N film. Remarkably, even after pausing for 12 h and resuming the tribological test, the lubricant maintained the superlubricity state on the (CrNbTiAlV)N film surface, with the friction coefficient remaining virtually unchanged (Figure S8, Supporting Information). This finding suggests that irreversible tribochemical reactions may have occurred on the lubricant or the (CrNbTiAlV)N film surface. The average friction coefficients in the stable stage after the running-in period were all below 0.01, with the applied load ranging from 2 to 6 N, corresponding to the Hertz contact pressure ranging from 1.02 to 1.47 GPa (Figure 2c; Figure S9, Supporting Information). Moreover, as the load increased from 2 to 6 N, the running-in period progressively diminished (Figure \$10, Supporting Information). This phenomenon may be attributed to the facilitation of tribochemical reactions due to the increased pressure at the friction pair interface. When the load was 1 N, the pressure was likely too low for tribochemical reactions to occur, preventing the friction coefficient of the PA solution from decreasing below 0.01 within the 6000 s friction test duration. However, when the applied load increased to 7-8 N, the lubricating film between the two friction pair surfaces was prone to damage under relatively high pressure, resulting in friction coefficients exceeding 0.01. Additionally, the attainment of liquid superlubricity at various sliding speeds was systematically investigated. As illustrated in Figure 2d and Figure S11 (Supporting Information), when the sliding frequency increased from 2 to 5 Hz (corresponding to sliding speeds of 1.2-3.1 cm s⁻¹), the (CrNbTiAlV)N film lubricated with the PA solution achieved macroscopic superlubricity. Specifically, as the sliding frequency increased from 1 to 4 Hz, the average friction coefficient of this solid-liquid composite lubrication system decreased from 0.072 to 0.006, owing to the more favorable hydrodynamic lubrication at higher sliding speeds. When the sliding frequency further increased to 5 Hz, the average friction coefficient slightly increased to 0.007. This phenomenon bears a resemblance to the classical Stribeck curve. [7d,25] Furthermore,

.com/doi/10.1002/adma.202413781 by

com, Wiley Online Library on [30/11/2024]. See the Terms

on Wiley Online Library for rules of use; OA articles are governed by the applicable Creative Cor



uating the tribological performance of solid—liquid composite lubrication systems. b) Real-time friction coefficient curves for different solid—liquid composite lubrication systems. The applied external load was 2 N, and the sliding frequency was 4 Hz. c) The average friction coefficient of (CrNbTiAlV)N film lubricated with PA solution under different applied loads and a reciprocating sliding frequency of 4 Hz. d) The average friction coefficient of (CrNbTiAlV)N film lubricated with PA solution at various sliding frequencies under an external load of 2 N. e) The average friction coefficient corresponds to different friction pair combinations. The applied load for the friction test was 2 N, with a sliding frequency of 4 Hz. f) The real-time friction coefficient of (CrNbTiAlV)N film was lubricated with a PA solution throughout 1 250 000 sliding cycles under a load of 2 N and a sliding frequency of 4 Hz. The insets are the 3D profile and depth change map of surface wear on the (CrNbTiAlV)N film after the tribological test. g) Comparison of friction coefficient and wear rate of PA solution lubricated (CrNbTiAlV)N film surface with previous work.

the PA@(CrNbTiAlV)N solid–liquid composite lubrication system can still achieve macroscopic superlubricity under the rotational friction mode (5 N, 5.23 cm s $^{-1}$), with a friction coefficient of ≈ 0.007 . Additionally, the friction coefficient exhibits significant speed dependency (Figure S12, Supporting Information).

To evaluate the universality of the PA@(CrNbTiAlV)N solid—liquid composite superlubricating system, the upper friction pair was replaced with ceramic balls possessing a hardness comparable to (CrNbTiAlV)N film or metal balls exhibiting excellent corrosion resistance. When the PA solution was employed as the

15214055, O. Downloaded from https://onlinelblaray.wiley.com/doi/10.1002/adma_202413781 by -Shbboletb--member@advancebolchina.com, Wiley Online Library on [301110204]. See the Terms and Conditions (https://onlinelblaray.wiley.com/terms-and-conditions) on Wiley Online Library for rules of use; OA articles are governed by the applicable Centwive Commons in

lubricant, superlubricity was attained between (CrNbTiAlV)N films and SiC, ZrO2, 201 steel, 304 steel, 316 steel, and 440C steel. The lowest friction coefficient of ≈0.002 was observed when the upper friction pair was 440C steel (Figure 2e; Figure S13, Supporting Information). However, the relatively lower hardness glass (≈6 GPa) or copper (≈0.4 GPa) counterparts were prone to wear, generating abundant wear debris and resulting in higher surface roughness, failing to reach the superlubricating state (Figures S14 and S15, Supporting Information). More information on the mechanical and tribological properties of different friction pair materials can be found in Table S2 (Supporting Information). These findings demonstrate the versatility of this solid-liquid composite lubrication system in achieving superlubricity across diverse tribological pairs. Notably, the realization of macroscale superlubricity between engineering steel surfaces via this solid-liquid composite lubrication strategy holds immense promise for the future proliferation and practical implementation of superlubricity technology. The service life of superlubricity materials is another crucial parameter that necessitates evaluation, as it holds significant reference value for practical engineering applications. As illustrated in Figure 2f, after undergoing a running-in period, the friction coefficient of the PA@(CrNbTiAlV)N film solid-liquid composite solution remained below 0.01, with an average friction coefficient of ≈0.0037. In addition, the service life of this solid–liquid composite superlubricating system can endure for at least 1.25 million sliding cycles. After a total sliding distance of nearly 5 km, the maximum wear depth on the (CrNbTiAlV)N film was only 26.71 nm, corresponding to an ultra-low wear rate of 3.032×10^{-10} mm³·N⁻¹·m⁻¹. No significant wear was observed on the upper Si₃N₄ ball surface, indicating that this superlubricity system possesses a high load-bearing capacity (≈1.02 GPa) (Figure S16, Supporting Information). However, the CrNbTiAlV film lubricated with the PA solution and the (CrNbTiAlV)N film lubricated with phosphoric acid solution failed to achieve superlubricity within 180 000 friction cycles, and relatively deep wear tracks appeared on the film surfaces (Figures S17 and S18, Supporting Information). Figure 2g compares the friction coefficients and wear rates of this novel solid-liquid composite superlubricating system with those of previously reported superlubricating systems, including solid superlubricity, liquid superlubricity, and solid-liquid composite superlubricity. [7b,9a,b,13,26] Specific comparative information can be found in Table \$3 (Supporting Information). In summary, the PA@(CrNbTiAlV)N solid-liquid composite simultaneously achieved a robust superlubricity, a long lifetime, and an extremely low wear rate.

2.3. Characterization and Analysis of Lubricant and Wear Track After Friction Test

To gain deeper insights into the possible mechanisms underpinning the PA@(CrNbTiAlV)N solid–liquid composite superlubricating system, a comprehensive analysis of the lubricant and the wear track region was conducted after a friction test (**Figure 3a**). A substantial amount of in situ formed HEC nanoparticles were found in the post-tribotest lubricant, as shown in Figure 3b,c. In addition, the HEC nanoparticles exhibited a relatively uniform size distribution, with an average lateral dimension of \approx 7.3 nm

and a height of ≈5.7 nm, determined by using AFM and TEM. Notably, the HRTEM image in Figure 3d displays lattice fringes with a spacing of 0.321 nm, corresponding to the (0-13) plane of (CrNbTiAlV)O, indicating the surface oxidation of the HEC nanoparticles during the friction process.[17a,23] Considering the detection limit of EDS, we intentionally obtained the EDS spectrum of the agglomerated nanoparticles. The EDS analysis revealed that in addition to the uniformly distributed Cr, Nb, Ti, Al, V, and N elements, the agglomerated nanoparticles also exhibited a significant presence of O, further corroborating the surface oxidation of HEC nanoparticles to form (CrNbTiAlV)O (Figure 3e). In order to exclude the possibility that the nanoparticles originated from the PA solution, pure water was employed as the lubricant, a certain amount of HEC nanoparticles was also observed after the friction test (Figures \$19 and \$20, Supporting Information).

Then, the composition of the lubricant after the friction test was systematically analyzed. In contrast to the original PA lubricant (0 h, orange line), the absorption peak at 2766 cm⁻¹, attributed to the P-H stretching vibration of the phosphoric acid molecule, gradually became more prominent as the friction test progressed, as illustrated in Figure 3f. This observation indicates that during the friction process, the PA molecules in the lubricant are hydrolyzed to produce a certain amount of phosphoric acid molecules.^[27] The PA solution exhibited no significant changes in the corresponding absorption peaks after being statically placed on the (CrNbTiAlV)N coating surface for 12 h, suggesting that the friction process indeed accelerated the hydrolysis of PA molecules (Figure S21, Supporting Information). Furthermore, the ³¹P NMR spectrum of the PA solution after 12 h of friction test showed a marked change, becoming similar to that of a pure phosphoric acid solution, further substantiating the potential presence of phosphoric acid molecules in the lubricant after friction testing (Figure 3g).

Additionally, focused ion beam (FIB) milling combined with TEM was used to investigate the wear track region on the (CrNbTiAlV)N film lubricated by the PA solution (Figure S22, Supporting Information). As depicted in Figure 3h, a tribofilm with an approximate thickness of 22 nm was observed at the friction interface. The cross-section of the (CrNbTiAlV)N coating after friction testing exhibited a relatively smooth appearance, suggesting that the HEC nanoparticles present in the lubricant originated from the detachment of minute surface asperities on the (CrNbTiAlV)N coating due to the friction polishing action. To elucidate the potential chemical composition of the tribofilm, HRTEM images were obtained from two distinct regions within the tribofilm. As evident from Figure 3i, the region proximal to the (CrNbTiAlV)N film surface potentially underwent passivation under the combined effects of mechanical stress and frictional heat, resulting in the formation of a (CrNbTiAlV)O thin film with a thickness of a few nanometers. The measured lattice fringe spacing of 0.266 nm corresponds to the (01-4) plane of (CrNbTiAlV)O.[17a,23] Consistent with previous reports, [2c,14c] the upper region of the tribofilm also contained amorphous carbon, likely originating from adsorbed lubricant molecules on the friction surfaces. As shown in Figure S23 (Supporting Information), compared to the initial (CrNbTiAlV)N film, the worn area after friction testing exhibited two characteristic peaks at 1376 and 1560 cm⁻¹, corresponding to the D and G peaks of

15214095, 0, Downloaded from https://onlinelibrary.wiley.com/doi/10.1002/adma.202413781 by

com, Wiley Online Library on [30/11/2024]. See the Terms

ditions) on Wiley Online Library for rules of use; OA articles are governed by the applicable Creative

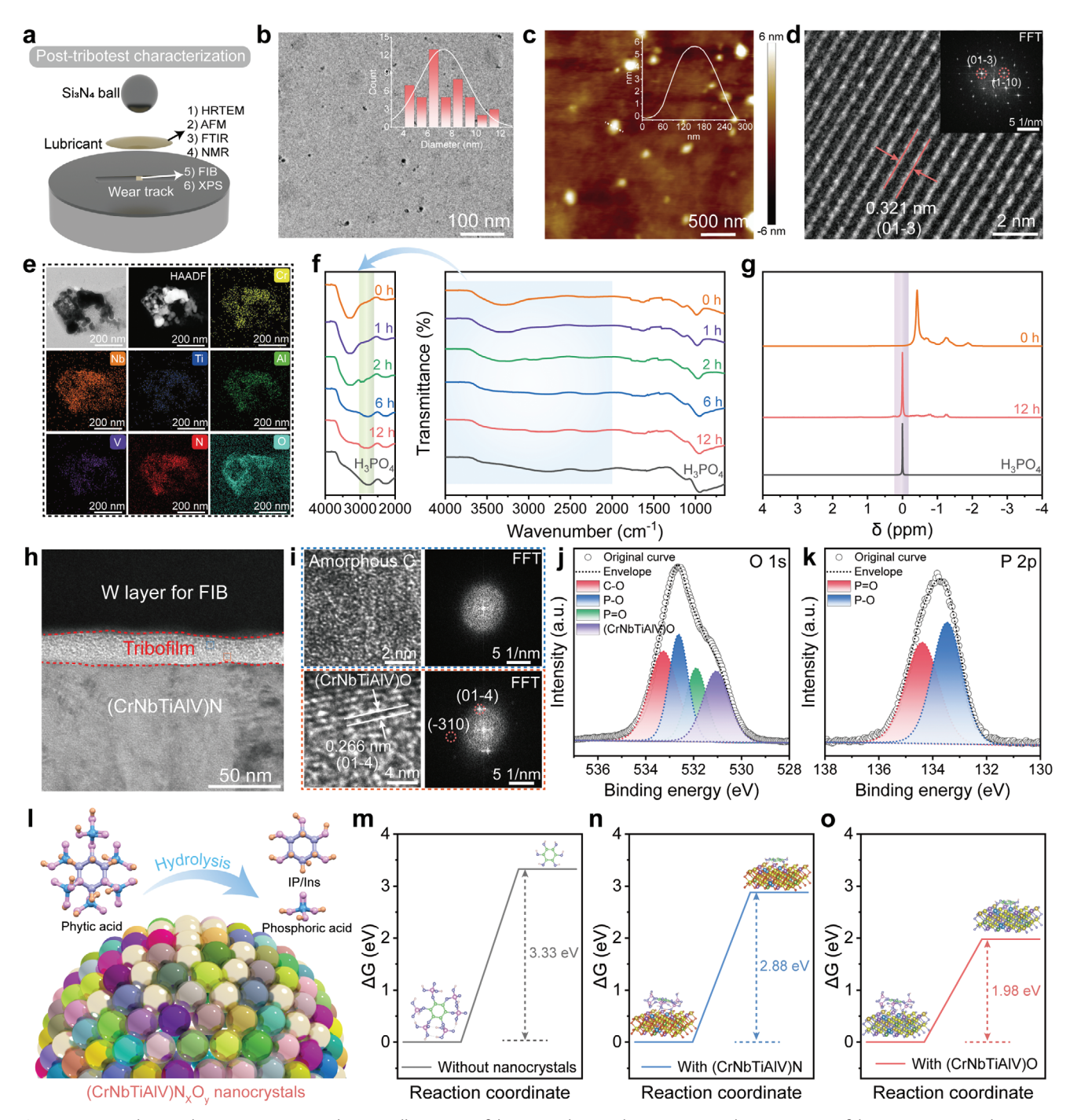


Figure 3. Post-tribotest characterization. a) Schematic illustration of the post-tribotest characterization. b) TEM image of the HEC nanocrystals present in the lubricant after friction tests. The upper right inset is the size distribution of the nanoparticles. c) AFM image of the HEC nanocrystals formed in situ during the friction process. The upper right inset shows the height profile of the nanocrystals. d) HRTEM image of the HEC nanocrystals. The upper right inset is the corresponding FFT image. e) EDS elemental mapping results of the agglomerated nanocrystals. f) FTIR spectrum of the lubricant after friction tests for different times. g) ³¹P NMR (400 MHz) spectra of the lubricant measured in heavy water before and after the friction test. h) TEM image of the cross-section of the wear marks on the surface of (CrNbTiAlV)N film lubricated by PA solution. i) HRTEM image and corresponding FFT image of a selected area of the wear track cross-section. XPS spectrum of the wear track on the surface of (CrNbTiAlV)N film after friction test: j) O 1s and k) P 2p. The four peaks observed at 533.3, 532.6, 531.9, and 531.1 eV in the XPS O 1s fine spectrum indicate the presence of C—O bonds, P—O bonds, P—O bonds, and (CrNbTiAlV)O, respectively. The P 2p peaks at 134.4 and 133.5 eV were attributed to P—O bonds and P—O bonds, respectively. l) Schematic diagram of the catalytic process of high-entropy ceramic nanocrystals on PA molecules. Free energy diagram for the dissociation of PA molecules m) without nanocrystals, n) with (CrNbTiAlV)N and o) with (CrNbTiAlV)O.

1521495.0, Downloaded from https://onlinelibtrary.wiley.com/doi/10.1002/adma.202413781 by Subboleth-memer@advancebelochina.com, Wiley Online Library on [30/11/2024]. See the Terms and Conditions (https://onlinelibtrary.wiley.com/terms-and-conditions) on Wiley Online Library for rules of use; OA articles are governed by the applicable Centwise Commons is a conditions.

amorphous carbon.^[14c] Additionally, analysis of the acquired electron energy loss spectra (EELS) revealed the presence of carbon π^* and σ^* peaks, further suggesting the potential existence of amorphous carbon in the friction film area (Figure S24, Supporting Information). [20b] XPS spectrums further corroborate the presence of adsorbed lubricant molecules and passivation-induced (CrNbTiAlV)O on the friction surfaces (Figure 3j,k).[7d,8,26a,e]

Based on the above analysis, we postulate that the in situ formed HEC nanoparticles (CrNbTiAlV) N_xO_y accelerated the hydrolysis of PA molecules into inositol polyphosphate (IP) or inositol (Ins) and phosphoric acid molecules (Figure 3l; Figure S25, Supporting Information). The possible equations for the hydrolysis process of PA molecules are as follows,

$$C_6H_{18}O_{24}P_6 \text{ (PA)} + nH_2O \xrightarrow{\text{(CrNbTiAlV)N}_xO_y} C_6H_{18-n}O_{24-3n}P_{6-n} \text{ (IP/Ins)} + nH_3PO_4$$
 (1)

To elucidate the effect of HEC nanoparticles on the hydrolysis of PA molecules, density functional theory (DFT) calculations were employed to determine the Gibbs free energy change (ΔG) required for the dissociation of PA molecules under three distinct scenarios. In the absence of HEC nanocrystals, the ΔG for the complete dissociation of PA molecules into inositol and phosphoric acid was calculated to be 3.33 eV (Figure 3m). However, in the presence of (CrNbTiAlV)N and (CrNbTiAlV)O HEC nanoparticles, the ΔG required for the hydrolysis of PA molecules was reduced to 2.88 and 1.98 eV, respectively (Figure 3n,o). These findings suggest that (CrNbTiAlV)N and (CrNbTiAlV)O HEC nanocrystals effectively accelerate the dissociation of PA molecules. In summary, the in situ HEC nanoparticles and the hydrolysis products of PA molecules, namely IP (or Ins) and phosphoric acid, potentially play a crucial role in achieving superlubricity.

2.4. The Mechanism of the Solid–Liquid Composite Super-Lubricating System

To infer the potential mechanisms and corresponding lubrication states underlying the superlubricity achieved in the solid-liquid composite system, the theoretical lubricating film thickness (h_c) between the (CrNbTiAlV)N film and Si₃N₄ ball was calculated to be \approx 9.92 nm based on the Hamrock–Dowson (H–D) theory.^[26e,g] Furthermore, from the ratio (0.89 < 1) between the film thickness and the equivalent roughness, we inferred that the lubrication regime corresponding to this solid-liquid composite superlubricating system is boundary lubrication (the detailed calculation process is available in the Supplementary information). Based on the post-tribotest characterization and film thickness calculation results presented above, a potential model for the achievement of superlubricity in this solid-liquid composite lubrication system is proposed, as shown in Figure 4. In the initial state of the friction test, the (CrNbTiAlV)N film was relatively rough with prominent asperities. The PA molecules were randomly distributed in the lubricant or partially adsorbed on the friction pair surfaces. As a complete boundary lubrication film was not yet formed on the friction pair surfaces, the PA@(CrNbTiAlV)N composite sys-

tem exhibited a relatively high friction coefficient (≈0.1) in the initial state (Figure 4a). As the friction test progressed, the asperities on the (CrNbTiAlV)N film surface gradually decreased in size due to the tribopolishing effect, leading to the in situ formation of HEC nanocrystals with a size of ≈6–8 nm. Possessing excellent catalytic performance, these in situ HEC nanocrystals can effectively accelerate the hydrolysis of the PA molecules, gradually forming IP (or Ins) and phosphoric acid molecules. Additionally, a few-nanometer-thick (CrNbTiAlV)O layer forms on the surfaces of the HEC friction pair and the generated nanocrystals, which can further reduce the energy required for the hydrolysis of PA molecules, thereby further promoting the hydrolysis process (Figure 4b). As shown in Figure 4c, the gradually hydrolyzed phosphoric acid and IP (or Ins) molecules adsorb onto the surface of the friction pair, effectively avoiding direct contact with surface rough peaks, reducing frictional resistance during the sliding process, and minimizing surface wear of the film. [26d,e] According to other studies, [9b,25] the in situ generated HEC nanocrystals can act as nano-additives to reduce friction and enhance wear resistance. Moreover, the surface of these nanocrystals may also fix a portion of water molecules, forming a hydration layer that can further reduce shear resistance and enhance boundary lubrication performance. [9b] In summary, the achievement of macroscopic superlubricity in this solid-liquid composite lubrication system is attributed to the combined effects of tribopolishing, the formation of HEC nanocrystals, and the hydrolysis products of the PA molecules.

To further validate the tribocatalytic effect of the (CrNbTiAlV)N HEC nanocrystals on PA molecules and the changes in friction performance of this lubrication system before and after the tribocatalytic effect, we performed both ab initio molecular dynamics (AIMD) simulations and classical molecular dynamics simulations. First, we employed AIMD simulations to investigate the evolution of PA molecules on the (220) surface of (CrNbTiAlV)N. As shown in Figure 5a, under the catalytic action of (CrNbTiAlV)N, the phosphate group on the PA molecule gradually began to detach after 5460 fs to form IP. Additionally, at 5706 fs, we observed that the detached phosphoric acid molecule may adsorb onto the (CrNbTiAlV)N surface. This result further confirms our hypothesis regarding the tribocatalysis effect of (CrNbTiAlV)N and is consistent with the experimental characterization results obtained after the friction test. More detailed information on the parameter settings from the AIMD simulations can be found in Supporting Information, and the specific real-time evolution process can be found in Movie S1 (Supporting Information).

In the proposed superlubricity mechanism, we hypothesized that the hydrolysis products (IP or Ins and phosphoric acid molecules) of PA molecules play a crucial role in achieving superlubricity. To validate this hypothesis, classical molecular dynamics simulations were performed to model the friction behavior of the lubrication systems before and after the tribocatalysis effect. For the simulation system before the tribocatalysis effect, the top and bottom friction layers were composed of $\mathrm{Si}_3\mathrm{N}_4$ and (CrNbTiAlV)N, respectively. The lubricant layer is composed of PA and water molecules. For the simulation system after the tribocatalysis effect, based on the characterization results obtained after friction testing, we replaced the bottom friction layer with (CrNbTiAlV)O, and the lubricant layer is consisted of inositol

com/doi/10.1002/adma.202413781 by

com, Wiley Online Library on [30/11/2024]. See the Terms

on Wiley Online Library for rules of use; OA articles are governed by the applicable Creativ-

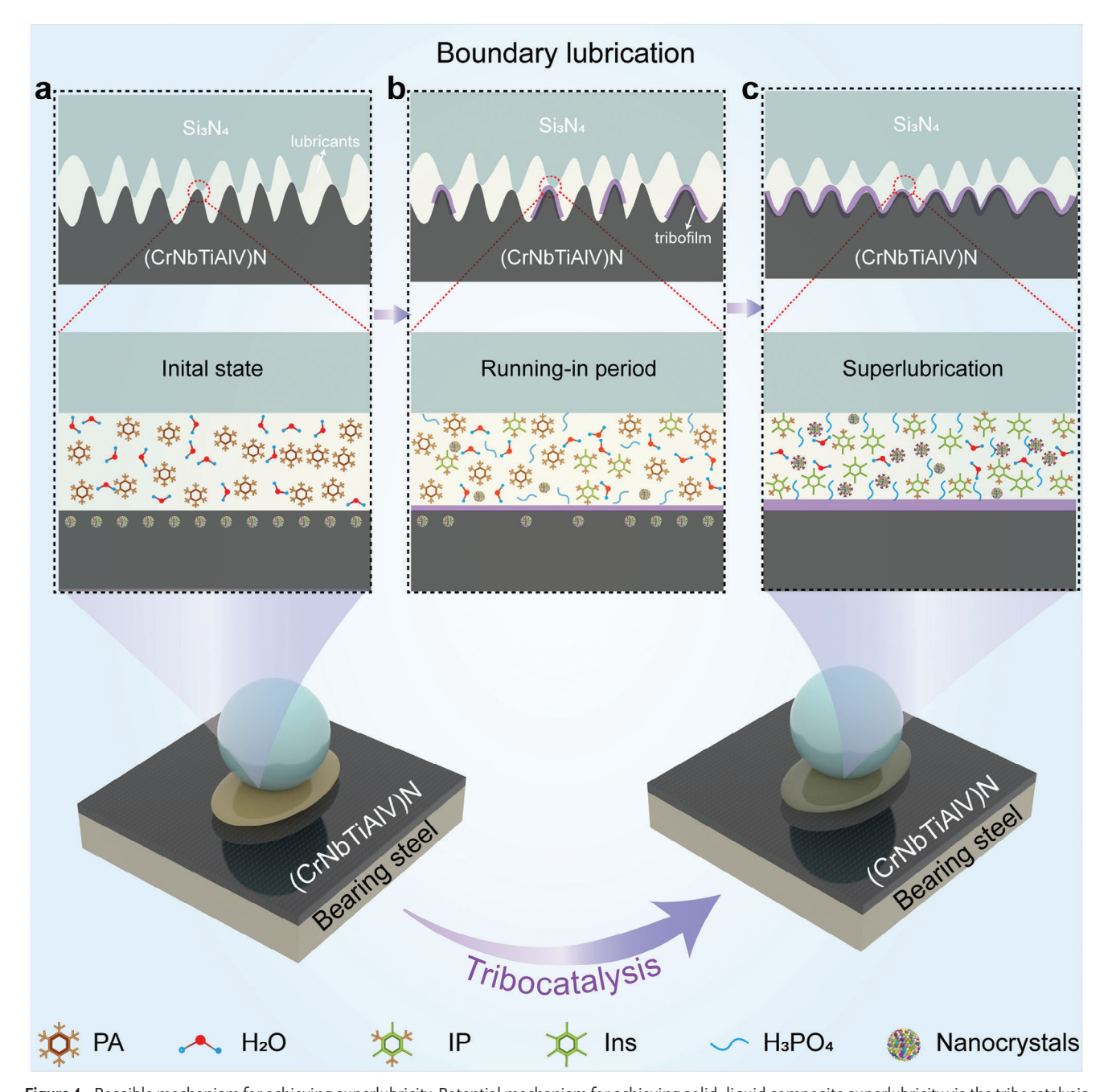


Figure 4. Possible mechanism for achieving superlubricity. Potential mechanism for achieving solid-liquid composite superlubricity via the tribocatalysis effect between the PA solution and the (CrNbTiAlV)N nanocomposite film: a) initial stage, b) running-in stage and c) superlubrication stage.

molecules, phosphoric acid molecules, and water molecules. As can be seen from Figure 5b and Movie S2 (Supporting Information), in the simulation system before the tribocatalysis effect, the PA molecules are mainly distributed randomly on the surface of the (CrNbTiAlV)N, with only a few PA molecules lying flat on the surface. In contrast, in the simulation system after the tribocatalysis effect, the inositol molecules are predominantly arranged parallel to the (CrNbTiAlV)O surface, resembling a 2D material (Figure 5c; Movie S3, Supporting Information). These different arrangements of the lubricant molecules in the two friction simulation systems may lead to differences in their friction performance. As shown in Figure 5d, the simulation system after the tribocatalytic effect exhibits a relatively lower friction coefficient, which is ≈47% lower than the friction coefficient before the tribocatalytic effect. To understand the reasons behind the changes in friction coefficient between these two simulation systems, we captured the evolution of the motion of PA molecules or inositol molecules that were initially arranged parallel to the friction layer surface in region 1 of the respective systems. For the simulation system before the tribocatalytic effect, the PA molecules

ununu advimat de

15214095, 0, Downloaded from https://onlinelibrary.wiley.com/doi/10.1002/adma.202413781 by <Shibb

com, Wiley Online Library on [30/11/2024]. See the Terms

) on Wiley Online Library for rules of use; OA articles are governed by the applicable Creative Commons

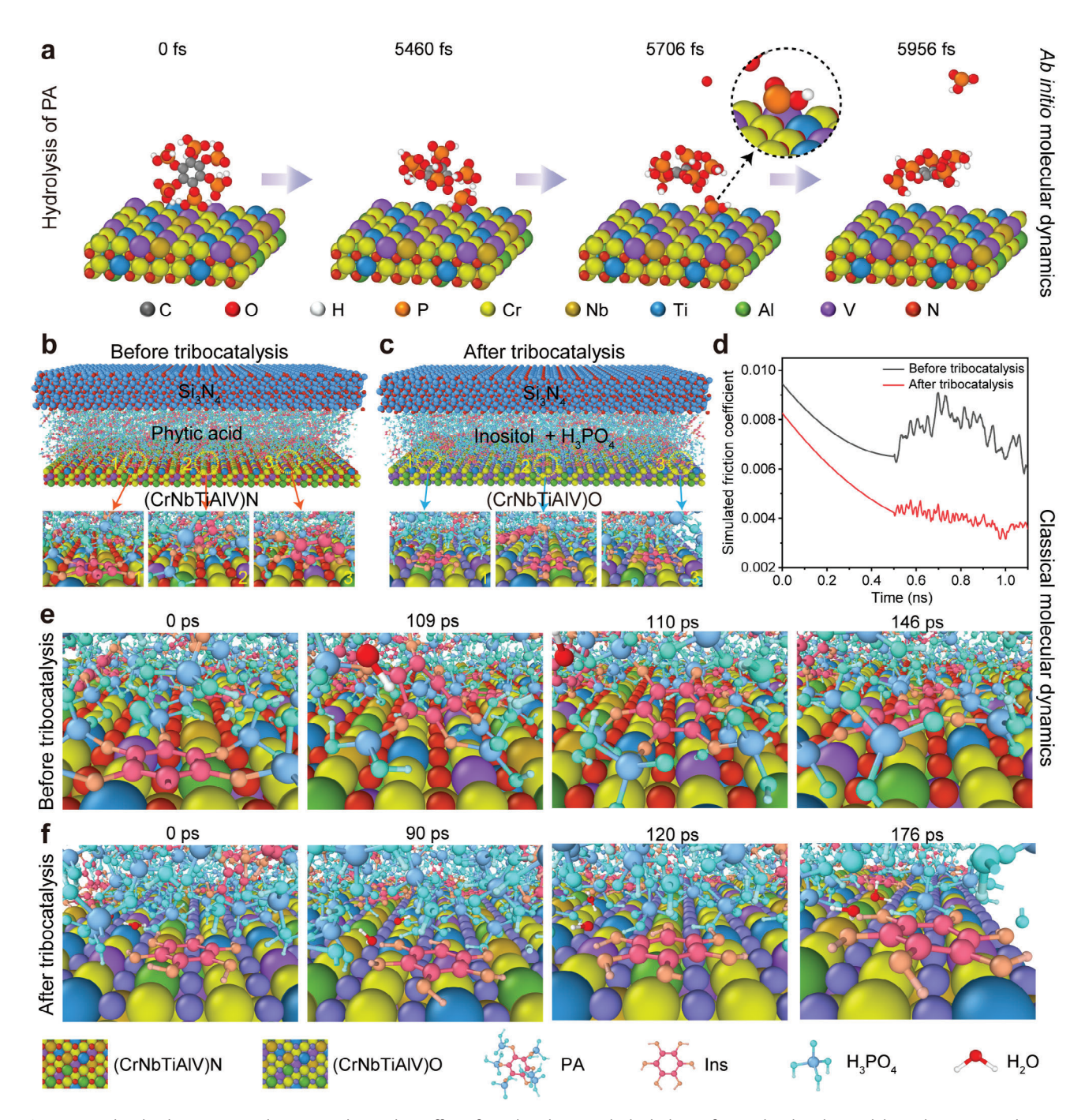


Figure 5. Molecular dynamics simulations. a) The catalytic effect of (CrNbTiAlV) N on the hydrolysis of PA molecules obtained through AIMD simulations. The overview and magnified regional views of the two friction simulation systems b) before and c) after the tribocatalysis effect obtained through classical molecular dynamics simulations. d) Simulated friction coefficient curves of two different friction simulation systems. The atomic snapshots at selected time frames of specific molecules in region 1 of the overview schematics for the two simulation systems: e) before tribocatalysis and f) after tribocatalysis.

initially lying flat on the friction layer surface underwent continuous flipping motions on the (CrNbTiAlV)N surface during the sliding process rather than sliding forward parallel to the friction layer surface. The flipping motion of PA molecules may lead to increased frictional resistance during the sliding process, resulting in a larger friction coefficient (Figure 5e). In contrast, after the

tribocatalytic effect, the inositol molecules initially arranged parallel to the HEC surface maintained their parallel configuration, sliding forward like graphene sheets until they exited the friction interface. This parallel sliding motion could be one of the main reasons for the reduced friction force during the sliding process (Figure 5f).^[28] Furthermore, partially detached phosphoric acid

15214095, 0, Downloaded from https://onlinelibrary.wiley.com/doi/10.1002/adma.202413781 by <Shibboleth

member@advancebiochina.com, Wiley Online Library on [30/11/2024]. See the Terms and Conditions (https://onlinelibrary.wiley.com/terms

and-conditions) on Wiley Online Library for rules of use; OA articles are governed by the applicable Creative Commons

molecules during sliding continue to adsorb onto the HEC surface, thus acting as boundary lubricants (Figure \$26, Supporting Information). In summary, these findings further demonstrate that the inositol and phosphoric acid molecules produced after the tribocatalytic effect can further reduce the friction coefficient of this solid—liquid composite lubrication system, thereby contributing to the achievement of macroscale robust superlubricity. In other words, the short-chain molecules or tribochemical reaction products formed after the catalytic effect of the lubricant may be more conducive to enhancing lubrication performance.

3. Conclusion

In summary, the novel solid-liquid composite superlubricity system constructed from the (CrNbTiAlV)N film and PA lubricant demonstrated an exceptionally prolonged operational lifetime and negligible wear rates. The outstanding mechanical properties and corrosion resistance of the (CrNbTiAlV)N film prevented severe wear or corrosion at the frictional interfaces, thereby averting the failure of superlubricity performance. Furthermore, a synergistic combination of experimental and simulation studies unveiled that the in situ formed HEC nanocrystals during the frictional process catalyzed the hydrolysis of PA molecules in the lubricant. The hydrolysis products, IP (or Ins) and phosphoric acid, together with the formation of an amorphous carbon film, were identified as the primary contributors to the realization of superlubricity. This research substantiates the feasibility of achieving ultra-low friction and wear performance through the tribocatalytic effect, providing a novel strategy for designing advanced solid-liquid composite superlubricity systems.

4. Experimental Section

Synthesis of (CrNbTiAlV) N Films: The (CrNbTiAlV) N high-entropy nitride film was synthesized on an AlSI52100 substrate using a magnetron sputtering system (UDP-650, Teer PlasMag). The Cr-Nb-Ti-Al-V composite splicing target was chosen, and nitrogen gas was selected as the reaction gas. Based on our previous research, the nitrogen gas flow rate during the deposition process was set to 38 standard cubic centimeters per minute (sccm). A bias voltage of $-126\,V$ was applied to the substrate during deposition, and the deposition time was 240 min. Additionally, as a comparative experiment, a CrNbTiAlV high-entropy alloy film was prepared with a nitrogen gas flow rate of 0 sccm during the deposition process. More detailed preparation procedures and process parameters are provided in Supporting Information.

Characterization of (CrNbTiAlV)N Films: The crystal structure of the (CrNbTiAlV) N film was analyzed using grazing incidence X-ray diffraction (GIXRD, Smartlab, Rigaku). The cross-sectional morphology and crystal structure of the film were observed through transmission electron microscopy (TEM, Talos F200X G2, FEI). Additionally, the elemental composition of the film cross-section was analyzed using an energy-dispersive spectrometer (EDS, Super-x, Thermo Scientific). HRTEM images of the samples were obtained using aberration-corrected scanningtransmission electron microscopy (Spectra 300, ThermoFisher). Sample preparation for TEM testing was carried out using a focused ion beam scanning electron microscope (FIB-SEM, Scios 2 HiVac, FEI). Atomic force microscopy (AFM, Multimode 8, Bruker) was employed in tapping mode to characterize the surface morphology and roughness of the film. The hardness and elastic modulus of the film were evaluated using a nanoindentation instrument (G200X, KLA, Berkovich tip). Furthermore, the adhesion strength between the film and the substrate was assessed using a scratch tester (MFT4000, Lanzhou Huahui Instrument).

Tribological Experiments: The friction experiments were conducted at room temperature (25 °C, 20–90% RH) using a ball-on-disk tribometer (TRB3, Anton Paar) in a linear reciprocating mode. The applied load during the friction tests ranged from 1 to 8 N, with a linear sliding amplitude of 2 mm and a sliding frequency of 0.5 Hz to 5 Hz (corresponding to sliding speeds of 0.3 to 3.1 cm s $^{-1}$). Subsequently, after the friction experiment, the depth, roughness and wear volume of the wear track were precisely measured using a 3D optical profilometer (UP-2000, Rtec Instruments).

Post-Tribotest Characterization: Characterization of wear spots and wear tracks on the surfaces of balls and disks was performed using optical microscopy (Axioscope 5, Zeiss, Germany). The wear tracks were cross-sectioned and thinned using FIB-SEM, and then the presence of tribofilm was confirmed using TEM. Lubricants collected after different friction test durations were characterized for changes in their chemical composition using Fourier transform infrared spectroscopy (FT-IR, Nicolet iS20, Thermo Scientific) and nuclear magnetic resonance (NMR, Avance NEO 400, Bruker). The microstructure and elemental distribution of in situ formed high-entropy nitride nanocrystals within the lubricant during the friction process were analyzed using TEM and EDS. The viscosity of the lubricants after the friction experiments was determined using a standard rotational rheometer (MCR302, Anton Paar). X-ray photoelectron spectroscopy (XPS, K-Alpha, Thermo Scientific) analysis was further employed to investigate the elemental composition and chemical states within the tribofilm in the wear track.

First-Principles Calculations: All calculations were conducted within the framework of density functional theory (DFT) employing the projector augmented plane-wave (PAW) method, as implemented in the Vienna ab initio simulation package. [29] The exchange-correlation potential was approximated using the generalized gradient approximation (GGA) proposed by Perdew, Burke, and Ernzerhof. [30] To account for dispersion effects, the Grimme D3 correction with a coordination number-dependent dispersion correction was applied. [31] The plane wave cutoff energy was set to 450 eV. For the iterative solution of the Kohn-Sham equation, an energy criterion of 10^{-5} eV was employed. To prevent artificial interactions between periodic images, a vacuum layer of 15 Å was included perpendicular to the sheet. Brillouin zone integration was performed using a $4 \times 4 \times 1$ k-mesh. [32] To ensure convergence, all structures were relaxed until the residual forces on the atoms decreased below 0.03 eV Å $^{-1}$. A dipole correction was applied for all slab models. Spin polarization is included in the calculations.

The Free energy changes (ΔG) of reaction intermediates could be calculated by the following:

$$\Delta G = \Delta E + \Delta E_{ZPE} - T\Delta S \tag{2}$$

where ΔE is the adsorption energy on the cluster surface from DFT calculations. The ΔE_{ZPE} and ΔS are the difference for the zero-point energy and entropy. The zero-point energy and entropy are calculated at the standard conditions corresponding to the pressure of 101 325 Pa (\approx 1 bar) of H₂ at the temperature of 298.15 K.

Molecular Dynamics Simulations: To obtain the atomic-scale evolution pathways of PA molecules on the (CrNbTiAlV)N (220) surface, we performed DFT-based ab initio molecular dynamics (AIMD) simulations in a typical canonical ensemble (NVT). The ensemble maintained constant particle number, volume, and temperature. The DFT calculations were carried out using the classical Vienna Ab initio Simulation Package (VASP).[33] The Perdew-Burke-Ernzerhof (PBE) generalized gradient approximation exchange-correlation functional was adopted. [30] A structure comprising the substrate and molecules was constructed, and periodic boundary conditions were applied, with a 20 Å vacuum layer in the z-direction to prevent inter-image interactions. A plane-wave cutoff energy of 500 eV was chosen to represent the electronic states accurately. The convergence criteria were set to 10^{-4} eV for energy and appropriate force values. For the Brillouin zone sampling, a $1 \times 1 \times 1$ k-point mesh was employed. The integration of Newton's equations of motion was facilitated by the widely adopted Verlet algorithm, with a time step of $\delta_t = 10^{-3}$ ps.

The evolution of lubricants from an atomistic perspective during the friction process before and after the tribocatalysis effect was investigated using classical molecular dynamics simulations. The classical molecular

www.advancedsciencenews.com

ADVANCED MATERIALS

www.advmat.de

dynamics simulations were performed in the canonical ensemble (NVT) using the LAMMPS software package.^[34] The PACKMOL software was used to build the initial system configuration.[35] The Velocity-Verlet algorithm was employed with an integration time step of 1.0 fs. The intermolecular interactions within the overall system were described using the PCFF force field. [36] Detailed potential parameters for transition metals (Cr, Nb, Ti, V) can be found in Table S4 (Supporting Information). [37] These parameters are set based on the LJ repulsive term to ensure the stability of the simulations. Temperature control was achieved through the Nosé-Hoover thermostat. $^{[38]}$ The Lorentz-Berthelot mixing rules were used to calculate the van der Waals (vdW) interactions between different atom types, with a cutoff distance of 1.2 nm for the vdW interactions. The particle-particleparticle-mesh (PPPM) method was employed to compute the long-range electrostatic interactions. Prior to the simulations, the entire system underwent an energy minimization process to generate a reasonable and stable model structure. During the relaxation process, the system was first heated from 10 to 300 K using the NVT ensemble throughout 0.5 ns. Subsequently, the system was equilibrated at 300 K for 1 ns to ensure the convergence of physical properties and the reliability of the simulation results. After equilibration, the top friction layer was moved along the positive xdirection with a velocity of 20 m s⁻¹ to mimic the actual friction process. The friction coefficient was calculated from the forces exerted on the top friction layer in the x and z directions during its motion.

Supporting Information

Supporting Information is available from the Wiley Online Library or from the author.

Acknowledgements

C.D., T.Y., and X.S. contributed equally to this work and should be considered co-first authors. Thanks for the financial support of the Strategic Priority Research Program of the Chinese Academy of Sciences (Grant No. XDB 0470103), the National Natural Science Foundation of China (52205230, U21A2046, 52275219, and 52205233), the Program for Taishan Scholars of Shandong Province (No. ts20190965), the Key Research Program of the Chinese Academy of Sciences (ZDBS-ZRKJZ-TLC010), the Western Light Project of CAS (xbzg-zdsys-202118), Major Science and Technology Projects in Gansu Province (No. 22ZD6GA002), the Major Program of the Lanzhou Institute of Chemical Physics CAS (No. ZYFZFX-5), the Key Research and Development Program in Shandong Province (No. SYS202203), the LICP International Cooperative Scholarship, and the LICP Cooperation Foundation for Young Scholars (HZJJ23-7 and HZJJ23-8) for providing financial support.

Conflict of Interest

The authors declare no conflict of interest.

Data Availability Statement

The data that support the findings of this study are available from the corresponding author upon reasonable request.

Keywords

high-entropy ceramic, nanocrystals, superlubricity, tribocatalysis, wear rate

Received: September 12, 2024 Revised: November 24, 2024 Published online:

- a) K. Holmberg, A. Erdemir, *Friction* 2017, 5, 263; b) K. Holmberg, P. Andersson, A. Erdemir, *Tribol. Int.* 2012, 47, 221; c) A. Rosenkranz, M. C. Righi, A. V. Sumant, B. Anasori, V. N. Mochalin, *Adv. Mater* 2023, 35, 2207757.
- [2] a) M. R. Cai, Q. L. Yu, W. M. Liu, F. Zhou, Chem. Soc. Rev. 2020, 49, 7753; b) D. Berman, A. Erdemir, A. V. Sumant, ACS Nano 2018, 12, 2122; c) D. Berman, A. Erdemir, ACS Nano 2021, 15, 18865.
- [3] a) O. Hod, E. Meyer, Q. S. Zheng, M. Urbakh, *Nature* 2018, 563, 485;
 b) J. Liu, X. Yang, H. Fang, W. Yan, W. Ouyang, Z. Liu, *Adv. Mater.* 2023, https://doi.org/10.1002/adma.202305072.
- [4] a) H. Li, J. Wang, S. Gao, Q. Chen, L. Peng, K. Liu, X. Wei, Adv. Mater. 2017, 29, 1701474; b) Z. Liu, J. R. Yang, F. Grey, J. Z. Liu, Y. L. Liu, Y. B. Wang, Y. L. Yang, Y. Cheng, Q. S. Zheng, Phys. Rev. Lett. 2012, 108, 205503; c) X. Huang, T. Li, J. Wang, K. Xia, Z. Tan, D. Peng, X. Xiang, B. Liu, M. Ma, Q. Zheng, Nat. Commun. 2023, 14, 2931; d) D. Berman, B. Narayanan, M. J. Cherukara, S. K. R. S. Sankaranarayanan, A. Erdemir, A. Zinovev, A. V. Sumant, Nat. Commun. 2018, 9, 1164; e) D. Berman, S. A. Deshmukh, S. K. R. S. Sankaranarayanan, A. Erdemir, A. V. Sumant, Science 2015, 348, 1118; f) X. Huang, X. Xiang, J. Nie, D. Peng, F. Yang, Z. Wu, H. Jiang, Z. Xu, Q. Zheng, Nat. Commun. 2021, 12, 2268; g) L. Zhang, H. Cai, L. Xu, L. Ji, D. Wang, Y. Zheng, Y. Feng, X. Sui, Y. Guo, W. Guo, F. Zhou, W. Liu, Z. L. Wang, Matter 2022, 5, 1532; h) X. Yang, R. Li, Y. Wang, J. Zhang, Adv. Mater 2023, 35, 2303580.
- [5] a) P. P. Li, P. F. Ju, L. Ji, H. X. Li, X. H. Liu, L. Chen, H. D. Zhou, J. M. Chen, Adv. Mater 2020, 32, 2002039; b) T. Yu, R. Shen, Z. Wu, C. Du, X. Shen, N. Jia, H. Deng, Y. Zhao, L. Zhang, Y. Feng, Z. Zhang, Y. Luo, F. Zhou, D. Wang, Nano Lett. 2023, 23, 1865.
- [6] T. Han, S. Zhang, C. Zhang, Friction 2022, 10, 1137.
- [7] a) J. J. Li, C. H. Zhang, J. B. Luo, Langmuir 2011, 27, 9413; b) T. Y. Han,
 S. Yi, C. H. Zhang, J. J. Li, X. C. Chen, J. B. Luo, X. Banquy, J. Colloid Interface Sci. 2020, 579, 479; c) X. Y. Ge, J. J. Li, C. H. Zhang, J. B. Luo, Langmuir 2018, 34, 3578; d) C. Du, T. Yu, L. Zhang, R. Shen, Z. Wu,
 X. Li, X. He, Y. Feng, D. Wang, Tribol. Int. 2023, 183, 108387.
- [8] C. Du, T. Yang, T. Yu, L. Zhang, X. Sui, Y. Feng, X. Wang, D. Wang, Adv. Funct. Mater. 2024, 34, 2310880.
- [9] a) J. Pan, K. Zhang, J. Wang, X. Gu, Q. Zhao, Y. Shan, M. Wen, C. Liu,
 W. Zheng, C. Chen, *Acta Mater.* 2024, 262, 119439; b) J. Wang, C. Liu,
 K. Miao, K. Zhang, W. Zheng, C. Chen, *Adv. Sci.* 2022, 9, 2103815; c)
 X. Xu, Q. Ma, C. Yan, M. Liang, H. Wang, *Carbon* 2024, 225, 119113.
- [10] a) T. Kuwahara, P. A. Romero, S. Makowski, V. Weihnacht, G. Moras, M. Moseler, *Nat. Commun.* 2019, 10, 151; b) Y. Long, J. Galipaud, V. Weihnacht, S. Makowski, J. M. Martin, M.-I. De Barros Bouchet, *Tribol. Int.* 2022, 169, 107462.
- [11] S. Sun, J. Li, J. Li, J. Luo, Carbon 2022, 199, 161.
- [12] S. Yi, J. Li, J. Rao, X. Ma, Y. Zhang, Chem. Eng. J. 2022, 449, 137764.
- [13] G. B. Tang, Z. B. Wu, F. H. Su, H. D. Wang, X. Xu, Q. Li, G. Z. Ma, P. K. Chu, Nano Lett. 2021, 21, 5308.
- [14] a) V. R. Salinas Ruiz, T. Kuwahara, J. Galipaud, K. Masenelli-Varlot, M. B. Hassine, C. Héau, M. Stoll, L. Mayrhofer, G. Moras, J. M. Martin, M. Moseler, M.-I. de Barros Bouchet, *Nat. Commun.* 2021, *12*, 4550; b) P. G. Grützmacher, M. Cutini, E. Marquis, M. Rodríguez Ripoll, H. Riedl, P. Kutrowatz, S. Bug, C.-J. Hsu, J. Bernardi, C. Gachot, A. Erdemir, M. C. Righi, *Adv. Mater.* 2023, *35*, 2302076; c) A. Erdemir, G. Ramirez, O. L. Eryilmaz, B. Narayanan, Y. Liao, G. Kamath, S. K. R. S. Sankaranarayanan, *Nature* 2016, *536*, 67.
- [15] J.-W. Yeh, S.-K. Chen, S.-J. Lin, J.-Y. Gan, T.-S. Chin, T.-T. Shun, C.-H. Tsau, S.-Y. Chang, Adv. Eng. Mater. 2004, 6, 299.
- [16] W.-L. Hsu, C.-W. Tsai, A.-C. Yeh, J.-W. Yeh, Nat. Rev. Chem. 2024, 8, 471
- [17] a) R. Chen, Z. Cai, J. Pu, Z. Lu, S. Chen, S. Zheng, C. Zeng, J. Alloys Compd. 2020, 827, 153836; b) C.-H. Lai, S.-J. Lin, J.-W. Yeh, S.-Y. Chang, Surf. Coat. Technol. 2006, 201, 3275; c) C. Zhang, X. Lu, C.



www.advancedsciencenews.com

ADVANCED MATERIALS

www.advmat.de

15214095, 0, Downloaded from https://onlinelibrary.wiley.com/doi/10.1002/adma.202413781 by

Wiley Online Library on [30/11/2024]. See the Terms

on Wiley Online Library for rules of use; OA articles are

governed by the

applicable Creative Common

- Wang, X. Sui, Y. Wang, H. Zhou, J. Hao, J. Mater. Sci. Technol. 2022, 107. 172.
- [18] X. Feng, K. Zhang, Y. Zheng, H. Zhou, Z. Wan, Mater. Chem. Phys. 2020, 239, 121991.
- [19] C. Zhang, X. Lu, H. Zhou, Y. Wang, X. Sui, Z. Shi, J. Hao, Surf. Coat. Technol. 2022, 429, 127921.
- [20] a) J. X. Yang, B.-H. Dai, C.-Y. Chiang, I. C. Chiu, C.-W. Pao, S.-Y. Lu, I. Y. Tsao, S.-T. Lin, C.-T. Chiu, J.-W. Yeh, P.-C. Chang, W.-H. Hung, ACS Nano 2021, 15, 12324; b) Y. Yao, Z. Huang, P. Xie, S. D. Lacey, R. J. Jacob, H. Xie, F. Chen, A. Nie, T. Pu, M. Rehwoldt, D. Yu, M. R. Zachariah, C. Wang, R. Shahbazian-Yassar, J. Li, L. Hu, Science 2018, 359, 1489; c) Q. Wang, X. Liu, D. He, D. Wang, Mater. Today 2023, 70, 218
- [21] Y. Zhai, X. Ren, B. Wang, S. Liu, Adv. Funct. Mater. 2022, 32, 2207536.
- [22] Y. Xu, G. Li, Y. Xia, Appl. Surf. Sci. 2020, 523, 146529.
- [23] D.-C. Tsai, Z.-C. Chang, B.-H. Kuo, M.-H. Shiao, S.-Y. Chang, F.-S. Shieu, Appl. Surf. Sci. 2013, 282, 789.
- [24] D. Niu, C. Zhang, X. Sui, X. Lu, X. Zhang, C. Wang, J. Hao, Z. Shi, Tribol. Int. 2022, 173, 107638.
- [25] H. Liang, M. Liu, T. Yin, S. Zou, X. Xia, X. Hua, Y. Fu, J. Zhang, Y. Bu, X. Ren, Adv. Funct. Mater. 2024, 34, 2311600.
- [26] a) X. Y. Ge, J. J. Li, C. H. Zhang, Z. N. Wang, J. B. Luo, Langmuir 2018, 34, 5245; b) G. Tang, F. Su, X. Liu, Z. Liang, T. Zou, P. K. Chu, Appl. Surf. Sci. 2023, 613, 156030; c) H. Liang, X. Chen, Y. Bu, M. Xu, G. Zheng, K. Gao, X. Hua, Y. Fu, J. Zhang, Friction 2023, 11, 567; d) C. Du, T. Yu, Z. Wu, L. Zhang, R. Shen, X. Li, M. Feng, Y. Feng, D. Wang, Friction 2023, 11, 748; e) C. Du, T. Yu, L. Zhang, H. Deng, R. Shen, X. Li, Y. Feng, D. Wang, ACS Appl. Mater. Interfaces 2023, 15, 10302; f)

- X. Fu, L. Cao, Y. Wan, R. Li, Ceram. Int. 2021, 47, 33917; g) S. Sun, S. Yi, J. Li, Z. Ding, W. Song, J. Luo, ACS Appl. Mater. Interfaces 2023, 15, 19705; h) Y. Liu, B. Yu, Z. Cao, P. Shi, N. Zhou, B. Zhang, J. Zhang, L. Qian, Appl. Surf. Sci 2018, 439, 976; i) Z. Gong, C. Bai, L. Qiang, K. Gao, J. Zhang, B. Zhang, Diamond Relat. Mater. 2018, 87, 172; j) K. Wang, B. Yang, B. Zhang, C. Bai, Z. Mou, K. Gao, G. Yushkov, E. Oks, Diamond Relat. Mater. 2020, 107, 107873; k) Q. Yu, X. Chen, C. Zhang, C. Zhang, W. Deng, Y. Wang, J. Xu, W. Qi, Friction 2022, 10, 1967.
- [27] L. Barrientos, J. J. Scott, P. Murthy, Plant Physiol. 1994, 106, 1489.
- [28] R. C. Sinclair, J. L. Suter, P. V. Coveney, Adv. Mater. 2018, 30, 1705791.
- [29] G. Kresse, D. Joubert, Phys. Rev. B 1999, 59, 1758.
- [30] J. P. Perdew, K. Burke, M. Ernzerhof, Phys. Rev. Lett. 1996, 77, 3865.
- [31] S. Grimme, J. Antony, S. Ehrlich, H. Krieg, J. Chem. Phys. 2010, 132, 154104.
- [32] D. J. Chadi, Phys. Rev. B 1977, 16, 1746.
- [33] a) G. Kresse, J. Furthmüller, Phys. Rev. B 1996, 54, 11169; b) G. Kresse, J. Furthmüller, Comput. Mater. Sci. 1996, 6, 15.
- [34] S. Plimpton, J. Comput. Phys. 1995, 117, 1.
- [35] L. Martínez, R. Andrade, E. G. Birgin, J. M. Martínez, J. Comput. Chem. 2009, 30, 2157.
- [36] H. Heinz, T.-J. Lin, R. Kishore Mishra, F. S. Emami, Langmuir 2013, 29, 1754.
- [37] A. K. Rappe, C. J. Casewit, K. S. Colwell, W. A. Goddard III, W. M. Skiff, J. Am. Chem. Soc. 1992, 114, 10024.
- [38] N. Shuichi, Prog. Theor. Phys. Suppl. 1991, 103, 1.